Optical absorption of THz-field-driven and dc-biased quantum wells

A. V. Maslov* and D. S. Citrin*
Semiconductor Optics Theory Group, Department of Physics and Materials Research Center, Washington State University, Pullman, Washington 99164-2814
(Received 12 March 2001; published 18 September 2001)

Linear optical absorption in a quantum well driven by a growth-direction-oriented THz electric field is investigated. We show that if in addition to the THz field a dc bias field is applied to the quantum well, the optical absorption becomes much more sensitive to the presence of the THz field. This results in the emergence of multiple replicas in the absorption spectrum of biased quantum wells for a low-frequency (compared with the subband energy spacing) THz field. We consider undoped quantum wells and develop an approach that allows us to treat nonlinear effects in THz field strength. We discuss separately the optical absorption due to free-electron-hole pairs and due to excitons.

DOI: 10.1103/PhysRevB.64.155309 PACS number(s): 78.67.De, 42.65.−k

I. INTRODUCTION

Optics is widely used for long-haul communication of information and shows promise for use inside digital information-processing machines.[1] From these perspectives, semiconductors play a crucial role in the practical realizations since they offer an unprecedented possibility for tailoring their optical properties. There are several ways in which the optical properties of semiconductors can be tailored. One way is band-gap engineering, i.e., growing layered low-dimensional semiconductor structures (heterostructures) with prescribed electronic properties. In addition to that, one can use externally applied magnetic and electric fields for further tuning or for controlling the properties in time with time-varying fields. It is well known that a dc electric field oriented in the growth direction of a semiconductor quantum well (QW) changes the optical absorption.[2,3] Without the electron-hole interaction, the electric field induces a redshift of the absorption edge, leads to a reduction in the magnitude of the absorption near the edge, and results in the appearance of additional absorption steps due to transitions forbidden in the absence of the field. This is called the quantum-confined Stark effect (QCSE), and it constitutes the basis of the operation of an important class of electro-optic modulators.

In a typical electro-optical modulator, the dc field is turned on and off by electronic devices and this controls the optical absorption. The latent electronic components put the upper limit on the switching speed and thus the bandwidth of signals is extremely narrow. To use to the fullest the broad bandwidth afforded by silica optical fiber, one can employ multiple wavelengths to route information into different channels, as realized in the wavelength division multiplexing (WDM) technology. However, simple proliferation of channels in WDM systems leads to many problems. The most challenging problem appears to be the need for stable multi-frequency laser sources. Another approach is to eliminate insofar as possible the use of inherently slow electronics to modulate optical signals at high rates. This, in principle, can be done by exploiting THz fields, and it provides a strong motivation to study the optical properties of QW's under the influence of THz fields. The marriage of optical and terahertz technologies is particularly advantageous in semiconductors. Indeed, the optical transitions occur between the valence and conduction bands. The THz field can be in resonance with the subbands in either the conduction or valence band and thus can very efficiently modify the optical absorption. From the technological viewpoint, semiconductor heterostructures can easily be integrated with both electronic and optic devices. The recent development in solid-state THz sources[4] gives hope that the merger of optical and THz technologies will not take long to emerge.

The investigation of the effects of a modulating THz field on the optical properties of semiconductor heterostructures has only recently become a field of extensive exploration. Following the developments in atomic optics, some earlier studies applied a few-level model to study the effects of the intersubband field on the interband optical absorption.[5] Later, optical absorption in semiconductors including excitonic effects was studied. For example, Ref. 6 studies the optical absorption of a QW driven by a strong growth-direction-oriented THz field with injected carriers. Inclusion of many subbands in describing the optical absorption in semiconductors is important since the THz field can simultaneously couple several subbands, and the optical absorption can be changed quite significantly compared with the case when only two THz coupled subbands are considered.[8,9] It has been shown that the linear optical absorption in QW's in the presence of a THz field tuned at resonance with the subband splitting produces splitting of the excitonic line[8,6,9] similar to the well-known Autler-Town splitting in atomic physics.[7] A recent study[10] discussed the possibility of observing quenching of the optical absorption in bulk semiconductors using resonant THz fields. As well as the change in the absorption, the generation of optical sidebands has attracted attention. For example, the emission of optical sidebands from QW magnetoexcitons in the presence of an in-plane polarized THz field was reported in Refs. 11 and 12. A theoretical desription of the optical absorption and sideband emission for in-plane THz fields was given in Refs. 13 and 14. Due to the symmetry of the structure, only even sidebands can be generated. The breaking of this symmetry due to spin effects was discussed in Ref. 15; however, the magnitude of the generated first-order sidebands is rather small. Recently, the generation of first-order THz optical sidebands in asymmet-

ric coupled QW's when the THz field was oriented in the growth direction was realized.[16] Similar effects are expected in a symmetrically grown QW that is biased by a dc field. The optical absorption of such a QW is the focus of this paper. The advantage of dc-biased QW's over asymmetrically grown QW's is the possibility of straightforward control of the degree of asymmetry by the dc bias field. In addition, similar properties should be present if the dc field is intrinsic rather than externally applied. In the present study, we consider the optical properties of undoped QW's. We present the results of the near-band-gap optical absorption for both unbiased and biased QW's. Two cases are particularly interesting: (i) when the THz field is in resonance with an intersubband transition and (ii) when the THz frequency is very small compared with the QW intersubband transitions. In unbiased QW's, the effects of the THz field on the optical absorption are more likely to be observed for resonant THz fields, rather than for nonresonant THz fields. For biased QW's, both resonant and nonresonant THz fields can significantly change the optical properties. Particularly noteworthy is the case of nonresonant THz fields where the presence of several THz replicas of the absorption peaks are found.

The paper is organized as follows. Section II gives the theoretical model used to describe the optical properties of QW's, and it also gives the relation between the microscopic polarization components of the QW density matrix and macroscopic quantities such as reflection, transmission, and absorption coefficients. The optical absorption in QW's without excitonic effects (band-to-band absorption) is investigated in Sec. III and with excitonic effects in Sec. IV. Section V gives our conclusion. In the Appendix we give necessary details of the numerical integration.

II. GENERAL THEORY

Our goal in this section is to present a general theory for calculating the optical (interband) absorption of a QW that is subjected to a growth-direction-polarized electric field $F(t)$ as schematically shown in Fig. 1. The electric field can have in general both a dc (F_{dc}) and an ac (F_{ac}) component. The ac component is periodic in time, but not necessarily harmonic, with the frequency in the THz range. The approach can be conveniently split into several successive steps. First, we will describe the QW structure. Second, we will introduce the equation for the interband polarization components of the density matrix for the QW. Third, we will relate the microscopic quantities to experimentally accessible macroscopic quantities such as optical absorption.

For simplicity, we consider a GaAs QW with infinite barriers at $z=\pm L/2$ with z the growth axis ([001] direction). We take $L=150$ Å. The wave function for confined carriers in the QW is written as a product of the bulk Bloch states $u_\alpha(\mathbf{r})$ and a slowly varying envelope part as

$$\psi^n_{\alpha\mathbf{k}}(\mathbf{r})=u_\alpha(\mathbf{r})\varphi^n_\alpha(z)\frac{e^{i\mathbf{k}\cdot\mathbf{r}}}{\sqrt{A}}, \tag{1}$$

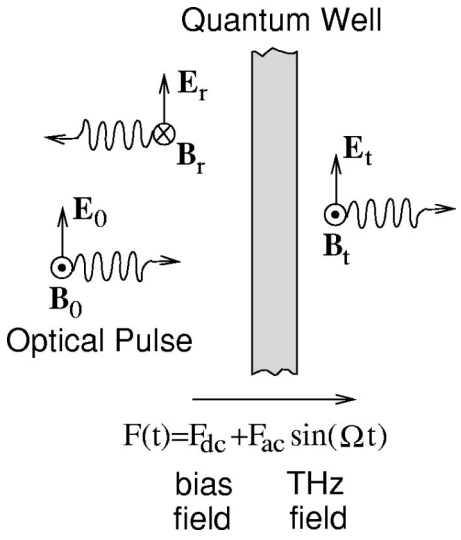

FIG. 1. Schematic representation of a normally incident optical pulse (with electric field E_0) onto a quantum well in the presence of a growth-direction-oriented electric field $F(t)$ with dc and ac components.

with α the carrier type (electron or hole), n the subband index, $\mathbf{k}$ the two-dimensional in-plane momentum, A the quantization area of the QW, and $\varphi^n_\alpha(z)$ the single-particle envelope functions. As a basis, we take the envelope functions that are eigenstates of the Hamiltonian for $F=0$:

$$\varphi^n_\alpha(z)=\sqrt{\frac{2}{L}}\begin{cases}\cos(n\pi z/L) & \text{if } n \text{ is odd}\\ \sin(n\pi z/L) & \text{if } n \text{ is even.}\end{cases} \tag{2}$$

The convenience of expanding the wave functions into the eigenstates of an unbiased QW stems from two factors. First, the Coulomb interaction between an electron and a hole depends on their separation and thus on their wave functions. A time-dependent field induces motion of the electron and the holes in their respective bands and the interaction between them becomes time dependent as well. Taking the wave functions of the unperturbed Hamiltonian, we avoid the difficulties of recalculating the time-dependent Coulomb matrix elements. Second, this representation allows us to treat both the dc and ac fields on the same footing, i.e., we do not need to recalculate the single-particle wave functions. However, we need to take several zero-field single-particle wave functions in order to describe correctly the optical properties associated with the transitions between the lowest conduction and valence subbands. Further, we will give justifications of our approach numerically. We consider only the heavy hole states. A more realistic calculation would include the light-hole states; however, for the aims of the present study, inclusion of only the heavy-hole subbands suffices. The material parameters are typical for GaAs:[17] $m_{h\parallel}=0.109m_0$, $m_{h\perp}=0.408m_0$, $m_{e\parallel}=m_{e\perp}=0.067m_0$, with m_0 the free electron mass. It is convenient to define the energy for free electrons (holes) with respect to the bottom (top) of the lowest (highest) state in the conduction (valence) band and to define the band-gap energy $\hbar\omega_g$ as the energy difference between the extremum states in the valence and conduction bands. The

free-particle energies are $\varepsilon^l_{\alpha\mathbf{k}}=\varepsilon^l_\alpha+\hbar^2\mathbf{k}^2/(2m_{\alpha\|})$ with $\varepsilon^l_{e(h)}=\hbar^2\pi^2(l-1)^2/(2L^2m_{e(h)\perp})$. In the numerical simulation we retain only two conduction subbands and four valence subbands.

To describe the carrier dynamics, we introduce creation $a^{l\dagger}_{\mathbf{k}}$, $b^{m\dagger}_{\mathbf{k}}$ and annihilation $a^l_{\mathbf{k}}$, $b^m_{\mathbf{k}}$ operators for electrons and holes, respectively, in subband l or m. All optical properties are characterized by the interband components of the density matrix $\langle b^m_{-\mathbf{k}}a^l_{\mathbf{k}}\rangle$. We employ the rotating-wave approximation relative to the band gap and introduce the slowly varying envelopes $p^{ml}_{\mathbf{k}}(t)$ defined as $\langle b^m_{-\mathbf{k}}a^l_{\mathbf{k}}\rangle=p^{ml}_{\mathbf{k}}(t)\exp(-i\omega_g t)$. The equation of motion for the slowly varying envelopes of the interband dipole matrix elements is obtained directly from the Hamiltonian,[18,9]

$$\frac{dp^{ml}_{\mathbf{k}}}{dt}=-\frac{i}{\hbar}(\varepsilon^l_{e\mathbf{k}}+\varepsilon^m_{h\mathbf{k}}-\hbar\omega_g)p^{ml}_{\mathbf{k}}+i\mathcal{E}(t)\delta_{lm}+\frac{i}{\hbar}F(t)\sum_n(\mu^{ln}p^{mn}_{\mathbf{k}}-\mu^{mn}p^{nl}_{\mathbf{k}})+\frac{i}{\hbar}\sum_{p,s,\mathbf{q}}V^{mp}_{ls}(\mathbf{k}-\mathbf{q})p^{ps}_{\mathbf{q}}-\Gamma_{\mathrm{sc}}p^{ml}_{\mathbf{k}}, \tag{3}$$

with $\mathcal{E}(t)$ the normalized slowly varying envelope of the real optical field $E(t)$ at the QW location such that

$$E(t)=\frac{\hbar\mathcal{E}(t)}{d_0}e^{-i\omega_g t}+\mathrm{c.c.} \tag{4}$$

where d_0 is the projection on the direction of the electric-field polarization (which is assumed linearly polarized) of the interband dipole matrix element between the conduction p-like and the valence s-like bulk Bloch states

$$d_0=ex_{cv}=e\int d\mathbf{r}\,u^*_e(\mathbf{r})xu_h(\mathbf{r}) \tag{5}$$

and $x_{cv}\approx(7/\sqrt{2})$ Å.[17] The coupling to the growth-direction polarized electric field

$$F(t)=F_{\mathrm{dc}}+F_{\mathrm{ac}}\sin\Omega t \tag{6}$$

is determined by the intersubband dipole matrix elements, which are defined for the electrons in the conduction band

$$\mu^{ln}=-ez^{ln}=-e\int_{-L/2}^{L/2}dz\,\varphi^l_e(z)z\varphi^n_e(z) \tag{7}$$

and for the wave functions (2) are

$$z^{12}=\frac{16L}{9\pi^2},\quad \frac{z^{14}}{z^{12}}=-\frac{18}{225},\quad \frac{z^{23}}{z^{12}}=-\frac{27}{25},\quad \frac{z^{34}}{z^{12}}=\frac{54}{49}.$$

Since we take the same confinement wave functions for the holes, the dipole elements will differ from those for electrons only by sign. The Coulomb matrix elements in Eq. (3) are

$$V^{mp}_{ls}(\mathbf{q})=\frac{2\pi e^2}{A\epsilon_b}\frac{f^{mp}_{ls}(q)}{q+\kappa}, \tag{8}$$

with the Coulomb overlap integrals

$$f^{mp}_{ls}(q)=\int_{-L/2}^{L/2}dz_e dz_h\varphi^l_e(z_e)\varphi^m_h(z_h)e^{-q|z_e-z_h|}\varphi^p_h(z_h)\varphi^s_e(z_e), \tag{9}$$

where ϵ_b is the background dielectric constant, and κ is the screening wave vector. The phenomenological dephasing Γ_{sc} in Eq. (3) is chosen to be k dependent: $\hbar\Gamma_{\mathrm{sc}}(k)=\hbar\Gamma_0(1+\alpha k/k_{\max})$, where $\hbar\Gamma_0=1$ meV (which corresponds to the characteristic polarization decay time of 0.66 ps), and we choose $\alpha=7$. Our model includes both F- and Coulomb-induced multisubband couplings in calculating the optical spectra. Without these couplings, Eq. (3) reduces to the polarization semiconductor Bloch equation (SBE) in the Hartree-Fock approximation.[18] The slowly varying envelope $\mathcal{P}(t)$ of the real macroscopic optical polarization per unit area of the QW

$$P(t)=\mathcal{P}(t)\exp(-i\omega_g t)+\mathrm{c.c.} \tag{10}$$

is related to the interband polarization matrix elements as

$$\mathcal{P}(t)=\frac{d_0^*}{A}\sum_{n,\mathbf{k}}p^{nn}_{\mathbf{k}}(t). \tag{11}$$

The relation (11) between the microscopic and macroscopic quantities allows us now to treat the propagation of light through the QW from the point of classical electrodynamics. We take the complex slowly varying envelope of the incident field in the form

$$\mathcal{E}_i(t)=\mathcal{E}_0e^{-t^2/\tau^2}e^{-i(\omega_0-\omega_g)t} \tag{12}$$

with the full width at half maximum of the energy of the pulse $\tau\sqrt{\ln 4}=1.177\tau$ and ω_0 the center frequency of the pulse. Integrating Maxwell's equations across the QW and taking into account that the QW width is much smaller than the wavelength, we immediately obtain boundary conditions for the fields. Neglecting the derivatives of the envelopes in the boundary conditions, we obtain the relation between the envelopes of the incident $\mathcal{E}_i(t)$, transmitted $\mathcal{E}_t(t)$, and reflected $\mathcal{E}_r(t)$ waves:[19]

$$\mathcal{E}_r=\frac{2\pi i\omega_g d_0}{\hbar c\sqrt{\epsilon_b}}\mathcal{P}\ \text{ and }\ \mathcal{E}_t=\mathcal{E}_r+\mathcal{E}_i. \tag{13}$$

Changing the summation over discrete k to integration in Eq. (11) and substituting it into Eq. (13) we arrive at

$$\mathcal{E}_r(t)=\frac{i\Gamma_{\mathrm{rad}}}{16}a_b^2\sum_n\int_0^\infty dk\,kp^{nn}_{\mathbf{k}}(t) \tag{14}$$

with

$$\Gamma_{\mathrm{rad}}=\frac{16\omega_g}{\sqrt{\epsilon_b}}\frac{|x_{cv}|^2}{a_b^2}\frac{e^2}{\hbar c} \tag{15}$$

the radiative broadening of QW excitons in an infinitely thin QW, i.e., $\Gamma^{-1}_{\mathrm{rad}}$ is the characteristic decay time of QW exciton polarization.[20] For the QW material parameters that we use, $\Gamma^{-1}_{\mathrm{rad}}=13.3$ ps. We note that the envelope of the optical field $\mathcal{E}(t)$, which enters into the polarization SBE (3), must be the

field at the QW location and it coincides with the transmitted field $\mathcal{E}_t(t)$. However, if the reflection from the QW is very small, which is the case if $\Gamma_{\rm rad} \ll \Gamma_{\rm sc}$, the field at the QW location differs from the incident field by the reflected field and thus this difference can be neglected. We define the optical absorption as the ratio of the energy irreversibly absorbed per unit area of the QW per unit time assuming *continuous wave* (cw) illumination. For such a case, the absorption of a single QW is

$$A(\omega) = -2\,\mathrm{Re}[r(\omega)], \tag{16}$$

where Re denotes the real part of the complex reflection coefficient $r = \mathcal{E}_r(\omega)/\mathcal{E}_0(\omega)$. The expression for the optical absorption (16) is the result for which we are looking. It deserves some important comments. Our approach to calculating the cw optical absorption is essentially a time-domain technique. For unmodulated QW's, the optical absorption can be obtained in two equivalent ways: using cw fields or by using a short optical pulse and taking the Fourier transform. The second approach is experimentally and computationally very attractive since it allows one to obtain all relevant optical properties with just one short pulse. These two approaches are not equivalent for modulated QW's. Certainly, in our case a cw field means a long pulse whose duration significantly exceeds the THz period, while a short pulse is a pulse whose duration can be comparable to or much less than the THz period. So, strictly speaking, if one wants to find the optical absorption one is bound to use long pulses and scan through frequency. However, we have recently proposed a technique that relates the data obtained with short optical pulses to the cw optical properties. This technique can be extremely convenient both in numerical simulations[21] and in experiments.[22] The basic idea behind the short-pulse technique is to use several pulses that arrive at some known phases of the THz field. The results for the optical absorption of modulated QW's presented in the paper were obtained using short pulses. This helps to reduce significantly the computational efforts in solving Eq. (3).

III. BAND-TO-BAND OPTICAL ABSORPTION

Before we include the excitonic effects let us investigate the optical absorption due to electron-hole pairs in the absence of excitonic effects. The band-to-band absorption can be obtained using the approach developed in the previous section if we neglect the Coulomb interaction.

A. Optical absorption in the presence of a dc field (QCSE)

In this section we recall the effect of a dc field on the optical absorption. Without the dc field, the optical absorption shows the simple staircaselike behavior. For an ideal QW with infinite barriers, each step function has the same magnitude and starts at an energy that is equal to the difference between the valence and conduction subbands with the same subband index. The transitions between subbands with different numbers are forbidden. To discuss how the dc field changes the picture, we for now will divert from our model and use the conventional approach[3] of using as a basis the single-particle wave functions $\phi_\alpha^n(z)$ which are the eigenstates of the Hamiltonian with the dc field. The presence of the dc field changes the single-particle wave functions and gives rise to transitions between the valence and conduction subbands with different subband indices. The approximation of a QW with infinite barriers allows exact calculation of the QW properties such as the confinement wave functions, subband energies, and energies and strengths of the optical transitions. We will later use these exact results to compare them with those obtained from the time-domain approach before we proceed to the optical properties of the QW in the presence of a THz field. This will help to estimate the field strengths at which the use of only a few zero-field single-particle wave functions works well. The calculated single-particle wave functions for electrons and holes are shown in Fig. 2. The change of the hole wave functions with the field is much more noticeable than that for electrons. This is due to the much smaller energy difference between the valence subbands compared with the conduction subbands. Figure 3 shows how the average position

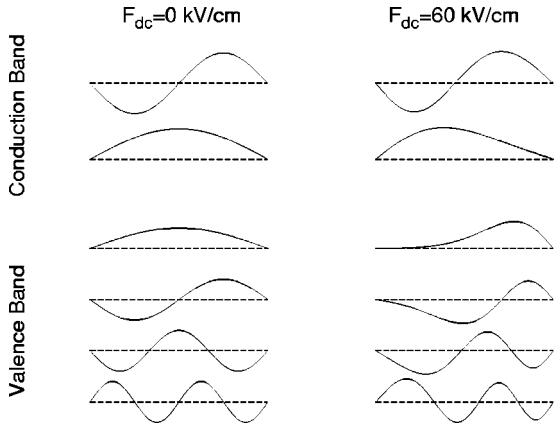

FIG. 2. Electron and hole wave functions for $F_{\rm dc} = 0$ kV/cm and $F_{\rm dc} = 60$ kV/cm.

$$\langle z_\alpha^n \rangle = \int_{-L/2}^{L/2} dz\, \phi_\alpha^n(z) z \phi_\alpha^n(z) \tag{17}$$

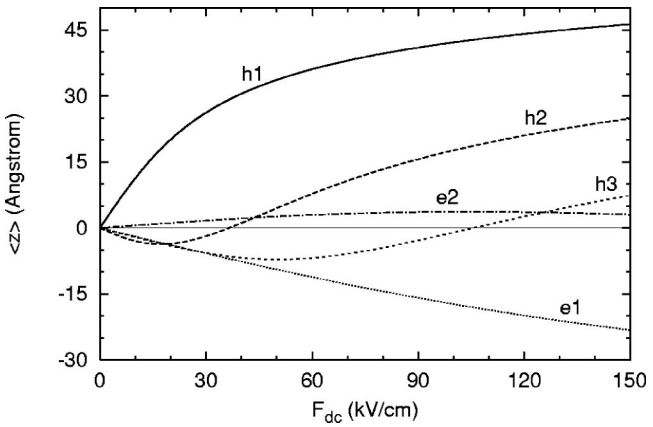

FIG. 3. Average electron and hole positions as a function of $F_{\rm dc}$.

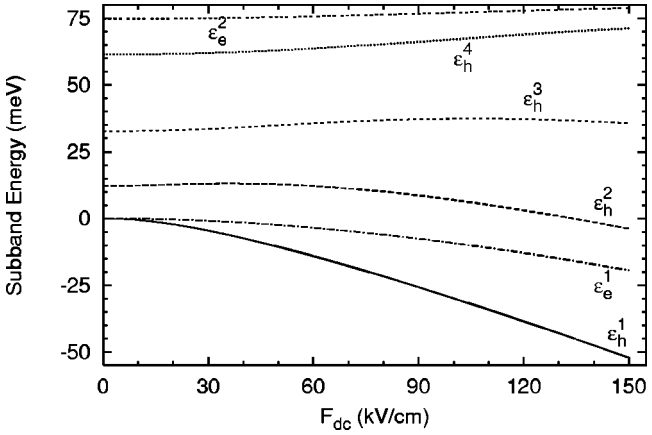

FIG. 4. Energies of the conduction and valence subbands as a function of F_{dc}.

of an electron and a hole in different subbands changes with the field. A hole (electron) in the lowest subband always moves along (against) the direction of the applied field for small F_{dc} while in all upper levels it moves against (along) the direction of the field. The change in the subband energies with F_{dc} is shown Fig. 4. Again, the change is much more pronounced for holes compared with that for electrons. The change in the subband energies gives rise to a change in the energy of the optical transitions. For convenience, we define the energy of the optical transitions ε^{nm} with respect to $\hbar\omega_g$ as $\varepsilon^{nm}=\varepsilon_h^n+\varepsilon_e^m$. Figure 5 shows the energies of the optical transitions. The overlap integrals between the wave functions in the valence and in the conduction bands are defined as

$$g^{nm}=\int_{-L/2}^{L/2} dz\ \phi_h^n(z)\phi_e^m(z) \tag{18}$$

and are shown in Fig. 6. The band-to-band absorption is completely characterized by the energy of the transition (Fig. 5) and the overlap integrals (Fig. 6) and can be written as

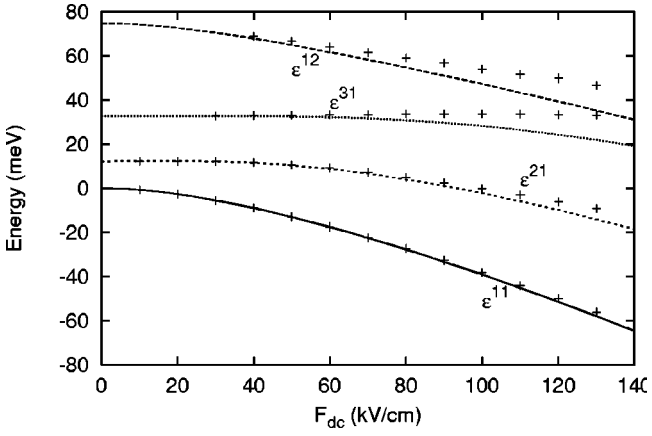

FIG. 5. Energies of several lowest optical transitions as a function of F_{dc}. The data points show the results obtained by keeping only the lowest four valence subbands and two conduction subbands.

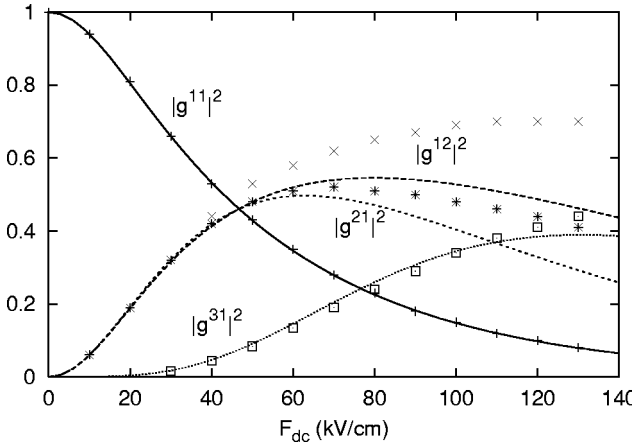

FIG. 6. Squares of the overlap integrals between the valence and conduction subbands. The data points show the results obtained by keeping only the lowest four valence subbands and two conduction subbands.

$$A(\omega)=A_0\sum_{n,m} g^{nm}\Theta(\hbar\omega-\varepsilon^{nm}) \tag{19}$$

where

$$A_0=\frac{2\pi}{\sqrt{\epsilon_b}}\frac{m_r}{m_0}\frac{\hbar\omega_g}{m_0c^2}\frac{|x_{cv}|^2}{\lambda_c^2}\frac{e^2}{\hbar c}, \tag{20}$$

$\lambda_c=\hbar/(m_0c)$ is the free-electron Compton wavelength, and $m_r=m_{h\|}m_{e\|}/(m_{h\|}+m_{e\|})$ is the relative electron-hole mass. The numerical value for the material parameters we use is $A_0=2.54\times10^{-3}$. The band-to-band optical absorption calculated using Eq. (19) near the band gap for different values of F_{dc} is shown in Fig. 7.

We now compare the exact results for the optical absorption shown in Figs. 5 and 6 with the results we obtained by using the time-domain approach and retaining four zero-field states in the valence band and two in the conduction band. To do this we calculated the optical absorption by integrating Eq. (3) in the presence of the dc field using a short optical pulse and then plotted the positions and the heights of the

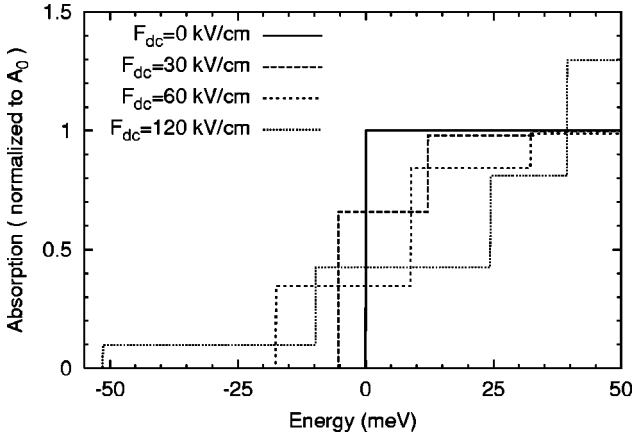

FIG. 7. Band-to-band optical absorption for $F_{\mathrm{dc}}=0,30,60,120$ kV/cm.

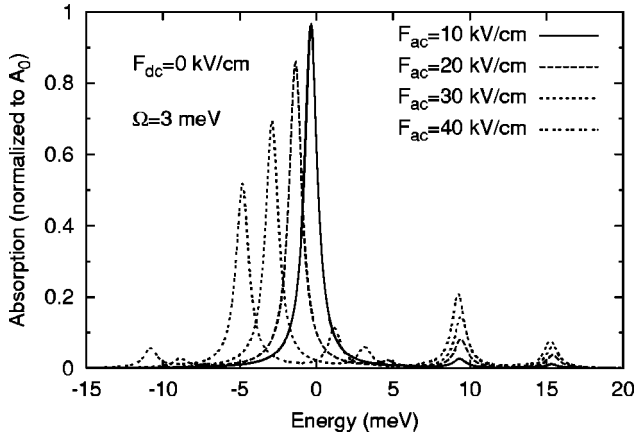

FIG. 8. Band-to-band optical absorption for $F_{dc}=0$, $F_{ac}=10,20,30,40$ kV/cm, and $\hbar\Omega=3$ meV. Peaks are used intead of steps.

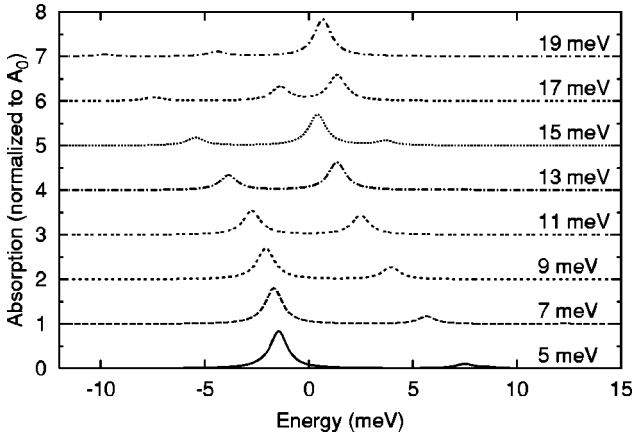

FIG. 9. Band-to-band optical absorption for $F_{dc}=0$, $F_{ac}=20$ kV/cm, and $\hbar\Omega=5,7,9,11,13,15,17,19$ meV. The spectra are displaced vertically for clarity and peaks are used intead of steps.

absorption steps as data points in Figs. 5 and 6, respectively. We can see that for the lowest optical transition our approximation is valid for dc fields as strong as 150 kV/cm while for the second optical transition it is correct up to $F_{dc} \lesssim 60$ kV/cm.

B. Optical absorption in the presence of a THz field

We now turn to the optical absorption in the presence of a THz field where we are going to use the time-domain approach whose validity we just discussed. In the presence of a THz field, the optical absorption will still be a set of step functions because the growth-direction-oriented field can couple only subband states with the same **k** and the sum over all **k** gives the two-dimensional density of states, which is a step function. So instead of plotting the step functions it is convenient to plot a narrow peak at the position of each step with its height equal to the height of the step function. It is equivalent to solving Eq. (3) only for the lowest states in each band, i.e., the $\mathbf{k}=\mathbf{0}$ states. Figure 8 shows the optical absorption, with peaks instead of step functions, in the presence of a THz field with $\hbar\Omega=3$ meV, which is much lower than the energy difference between the two lowest states in the valence band (12 meV). The phenomenological broadening of the peaks was $\hbar\Gamma_{sc}=0.5$ meV. Similar to the case of a dc field, the presence of a THz field gives rise to a redshift of the absorption edge and reduction of its height. However, both these effects are smaller compared with what one would observe with a dc field of the same strengh (compare with Figs. 6 and 5). More importantly, we can also observe the formation of replicas in the absorption spectrum. These replicas are not present for dc fields. One type of replica is separated from the main step (which is due to optically allowed transitions between the lowest conduction and valence subbands) by twice the THz frequency, which is taken to be 3 meV in Fig. 8. The replicas are not symmetric and the upper one is stronger than the lower. As well as the replicas on both sides of the main step, we can see significant steps separated by the THz frequency from the position of the second, optically forbidden, transition between the second valence and the first conduction subbands centered at about 12 meV. It is interesting that replicas can exist while the direct transtion itself does not. Similar to the replicas around the main step, the replicas around the second transition are asymmetric. However, in this case the lower-energy replica is significantly higher than the higher-energy one.

We now turn to the case when the THz frequency is close to the energy spacing between the two lowest valence subbands. Figure 9 shows the optical absorption in this case, with peaks instead of step functions, for different driving frequencies for $F_{ac}=20$ kV/cm. As the frequency of the THz field passes through the resonance at about 12 meV, the main step splits into two. The splitting is proportional to the field strength and at exact resonance the two steps have equal heights. For higher frequencies, at about 16 meV, the splitting occurs due to two-THz-photon coupling of the the first and the third valence subbands. Note that for such weak fields $F_{ac}=20$ kV/cm, no replicas are observed in the near-band-gap optical absoprtion spectrum.

C. Optical absorption in the presence of a dc field and a THz field simultaneously

Much richer optical absorption spectra can be obtained if the THz field drives a biased QW. Such a spectrum is shown in Fig. 10 for $F_{ac}=50$ kV/cm, $\hbar\Omega=3$ meV, and $F_{dc}=5,10,20$ kV/cm. Note that in the absence of the bias field the main effects we observed for such THz fields are a slight redshift of the main step accompanied by a slight reduction of the step height (see Fig. 8). In the presence of the dc field, we can clearly see multiple replicas on both sides of the main step and the second step. The replicas are separated from the steps by an integer number of the THz frequency. It is interesting that the first step can actually disappear completely and only replicas can remain. For relatively strong fields, there is a slight overall red shift in the position of the replicas and the main step. The origin of the high strength of the replicas can be understood from Fig. 5. The replicas appear due to the change in the position of the transition energy with the field. For a weak THz field the change of the energy of

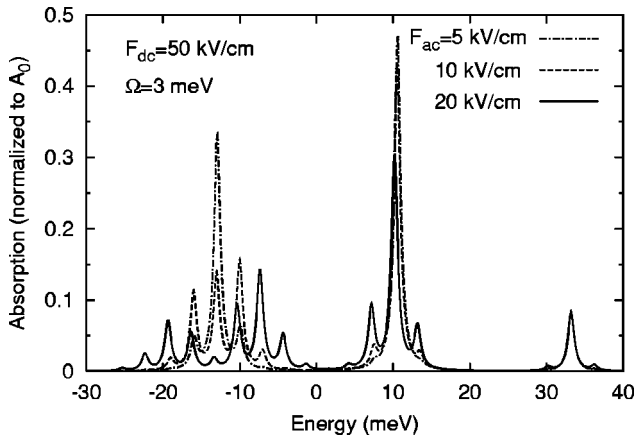

FIG. 10. Band-to-band optical absorption for $F_{dc}=50$ kV/cm, $F_{ac}=5,10,20$ kV/cm, and $\hbar\Omega=3$ meV. Peaks are used instead of steps.

the absorption peaks is simply the slope of the energy versus field curve. In the absence of the bias field, the energy of the lowest exciton transition changes quadratically with the field. For nonzero bias field, the change in the energy is linear with the field. For example, for $F_{ac}=10$ kV/cm, the change in the energy position of the lowest transition when $F_{dc}=0$ is roughly 0.7 meV while for $F_{dc}=50$ kV/cm it is 8 meV. The amplitude of the replicas around the first step as a function of the THz field strength is shown in Fig. 11. The main step decreases with the field and completely disappears at $F_{ac}=17$ kV/cm and starts to grow after that. The first replicas, separated by $\pm\hbar\Omega$ from the main step, initially increase with the field and then start to decrease. Higher-order replicas (separated by $\pm 2\hbar\Omega$) grow with the field for the field strengths shown in Fig. 11. Note that the replicas are asymmetric with the high-energy replicas being stronger than the lower-energy replicas. The assumption of adiabatic change in the energy of the lowest transition gives rise to symmetric replicas (with respect to the main peak). This is equivalent to the model used in calculations of multiphoton-assisted tunneling currents in superconducting diodes[23] where only the adiabatic change in the energy of the levels is used. The

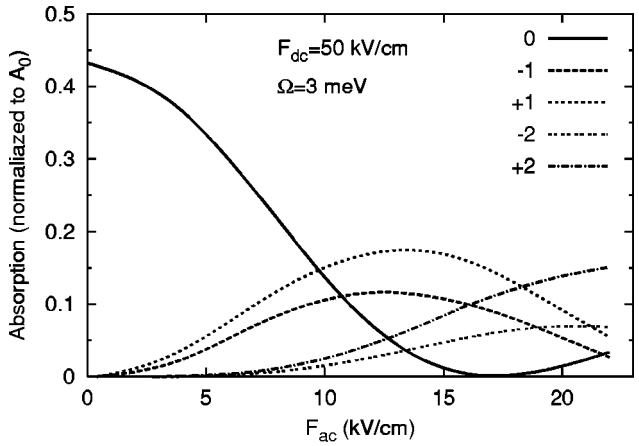

FIG. 11. Height of the main step and replicas $\pm 1,2$ around the main step shown in Fig. 10 as a function of F_{ac}.

asymmetry of the replicas comes from the fact that not only does the frequency of the transition level changes adiabatically with the THz field, but also the overlap integrals between the electron and the hole. Indeed, since the overlap decreases with the field strength (see Fig. 6), one expects the same order replicas to be higher for replicas with higher energy (i.e., on the right side of the main absorption step in Fig. 10) than for replicas with lower energy (on the left side of the main step). Another way to look at the origin of asymmetry is that the second level with which the first level interacts through the THz field lies above the first level, so the replicas above the first level are closer to the second level than the ones below.

In this section we study the band-to-band optical absorption. Due to the purely two-dimensional 2D density of states the absorption spectrum always shows the staircaselike behavior, although the position and height of the steps depend on the QW parameters, bias field, and amplitude and frequency of the THz field. In Figs. 8–10 we plotted the positions and the heights of the steps using peaks instead of steps. As well as the convenience, this is very illustrative in the following respect. For near-band-gap absorption, excitonic effects play a major role. So, instead of steps, one observes strong peaks due to the creation of bound electron-hole (e-h) states slightly below the expected position of the steps and slightly enhanced steps due to creation of correlated e-h pairs. At low temperatures the height of the excitonic absorption peaks exceeds the continuum absorption. So, strictly speaking, we expect that for QW's with strong excitonic properties we will observe absorption spectra that look qualitatively similar to the spikeslike behavior shown in Figs. 8–10, rather than exhibiting staircaselike behavior.

IV. EXCITONIC OPTICAL ABSORPTION

Having studied the optical absorption in a simple model that neglects the Coulomb interaction, we now turn to a more realistic model of the QW which includes the Coulomb interaction between the electron and the hole and thus correctly describes the optical absorption due to both bound and continuum e-h states. However, as we shall see in this section most of the effects we are going to see can already be understood qualitatively using the simpler model of Sec. III.

Figure 12 shows the QW absorption when the e-h Coulomb interaction is included. The numerical details are given in the Appendix. The absorption spectrum is dominated by exciton peaks rather than the step functions observed in the absence of e-h interaction (compare with Fig. 7). It is helpful to estimate the expected height of the exciton absorption peak in the absence of the bias field. In a very narrow QW the absorption due to the lowest lying exciton is

$$A=\frac{2\Gamma_{rad}\Gamma_{sc}}{(\omega-\omega_{exc})^2+\Gamma_{sc}^2}, \tag{21}$$

where ω_{exc} is the frequency of the lowest exciton state. The peak value of the absorption is $A=2\Gamma_{rad}/\Gamma_{sc}=9.9\times10^{-2}$ if $\Gamma_{rad}^{-1}=13.3$ ps and $\Gamma=0.66$ ps which is about five times higher than the value in Fig. 12. The discrepancy apparently comes from the fact that the thickness of the modeled QW is

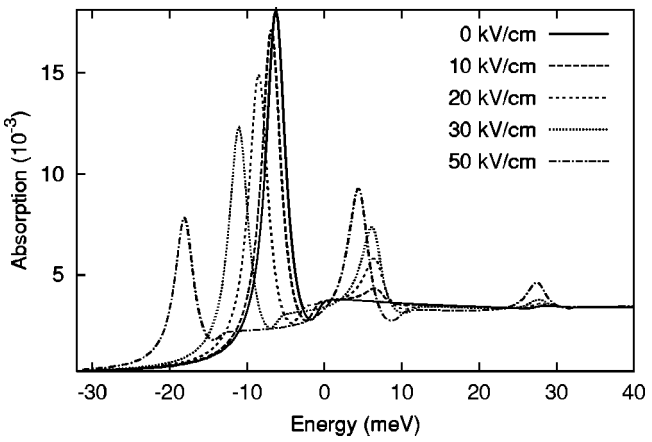

FIG. 12. Optical absorption including excitonic effects for $F_{\mathrm{dc}}=0,10,20,30,50$ kV/cm.

comparable to the bulk exciton Bohr radius and thus the exciton absorption is expected to be significantly lower in comparison with the purely 2D result. The variational calculations that we performed for the given QW show that the exciton radius is about 1.75 times larger compared with the pure 2D limit, which gives a reduction in the peak value by a factor of $1.75^2 \approx 3.1$. The *k*-dependent scattering rate and finite extent of the bands also contribute to the reduction of the peak absorption. Since our numerical results reproduce reasonably well some basic features of the QW absorption in the presence of the dc field with excitonic effects we can now proceed to study the effects of THz fields.

Figure 13 shows the optical absorption of an unbiased QW in the presence of a low-frequency THz field. Comparing the excitonic optical absorption with the results of the simple model in Fig. 8 we can see many similar features. The main excitonic peak shifts to the red and decreases in height with the field; replicas are formed around this peak; there are also two replicas around the position of the second excitonic peak while the peak is absent. Despite much qualitative agreement, the excitonic absorption shows that the presence of the continuum makes the replicas even more asymmetric.

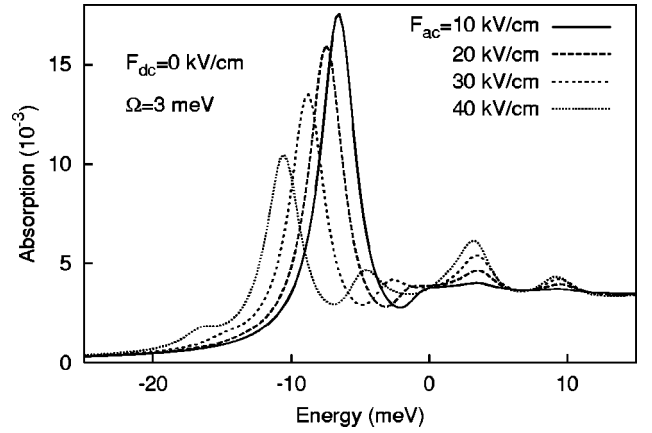

FIG. 13. Optical absorption including excitonic effects for $F_{\mathrm{dc}}=0$ kV/cm, $\hbar\Omega=3$ meV, and $F_{\mathrm{ac}}=10,20,30,40$ kV/cm.

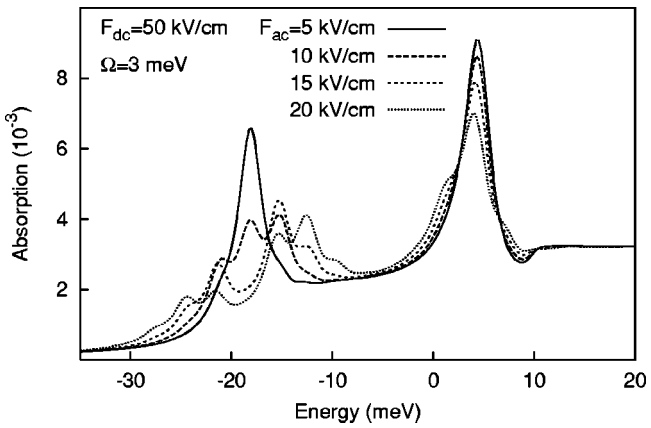

FIG. 14. Optical absorption including excitonic effects for $F_{\mathrm{dc}}=50$ kV/cm, $\hbar\Omega=3$ meV and $F_{\mathrm{ac}}=5,10,15,20$ kV/cm.

Figure 14 shows the optical absorption with $F_{\mathrm{dc}}=50$ kV/cm and different amplitudes of the THz field F_{ac} for a fixed value of the THz frequency. This result qualitatively resembles that of the simple model shown in Fig. 10. Due to relatively fast dephasing the replicas in Fig. 14 strongly overlap; however, they are definitely resolvable. As we can see from this figure, the excitonic peak decreases and multiple replicas appear as the THz field gets stronger. Again due to the presence of the continuum part of the absorption, the spectrum is very asymmetric. Figure 15 shows similar results as Fig. 14 but for a fixed THz field amplitude and different frequencies. For a low-frequency THz field, 2 meV, the central peak in Fig. 15 is absent and only two replicas exist. Apparently, if the frequency becomes even lower, i.e., $\Omega \lesssim \Gamma_{\mathrm{sc}}$ the replicas merge into one peak. If the THz frequency increases, a central peak appears and the replicas move away from the central peak. The replicas around the second peak are essentially unnoticeable. For high-frequency THz fields, resonance between the levels can occur. In this case we can observe splitting of the excitonic lines. However, for the given QW under a 50 kV/cm bias field, the splitting between the two lowest valence subbands becomes about 20 meV. For such high-frequency THz fields, coupling to optic phonons may become very important.

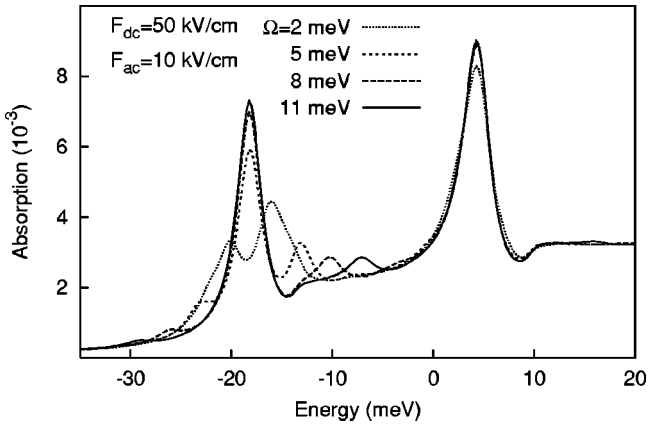

FIG. 15. Optical absorption including excitonic effects for $F_{\mathrm{dc}}=50$ kV/cm, $F_{\mathrm{ac}}=10$ kV/cm and $\hbar\Omega=2,5,8,11$ meV.

V. CONCLUSION

To conclude, we have studied the optical absorption in undoped QW's driven by a growth-direction-polarized THz electric field in the presence of a bias field. In the QW model that we used, the energy difference between the hole subbands is much smaller than that for the electron subbands. Thus, the growth-direction-polarized field mostly affects the hole subbands. Depending on the presence of the bias field and the frequency of the THz field, several regimes were discussed. First, we summarize the optical absorption in the absence of the bias. If the frequency of the THz field is below the resonance, its application causes a redshift of the lowest exciton peak and a reduction in its height. This is similar to the case of a dc field, although both the shift of the peak and the reduction of its height are smaller compared with the case of a dc field of the same strength. In addition, small replicas appear separated from the main peak by even numbers of the THz frequency. There are also replicas around the position of the forbidden transitions. These replicas are separated from the position of the transiton energy by an odd number of the THz frequency. For somewhat reasonable field stengths, such as 10–40 kV/cm, only first-order replicas are noticeable in the absorption spectrum. For THz fields close to the energy splitting between the subbands, we can observe rather complicated absorption spectra due to simultaneous mixing of several subbands by the THz field. In the simplest case when only resonance between two subbands occurs, the well known Autler-Towns splitting is recovered. More interesting effects are obtained when the THz field drives a biased QW. In this case, for a low-frequency THz field, multiple replicas appear around the lowest transition peak. We investigated the amplitude of the replicas as a function of the THz field strength and found that they behave nonmonotonically, which is a signature of the multi-THz processes that give rise to the replicas. Interestingly, the main exciton peak can completely disappear and only replicas remain. Our results were obtained using the polarization SBE in the linear regime with inclusion of excitonic effects in the optical absorption. We also investigated a simple model which allowed us to understand the results qualitatively.

ACKNOWLEDGMENTS

This work was supported by the Office of Naval Research and the National Science Foundation through Grants No. ECS-0072986, No. DMR9705403, and No. DMR-0073364.

APPENDIX A: CALCULATION OF THE COULOMB TERMS

Numerical evaluation of the Coulomb terms presents the most difficult part in solving Eq. (3). To simplify the Coulomb terms we use the symmetry of the interband polarization matrix elements, which allows explicit integration over the angle in the 2D Coulomb integral,

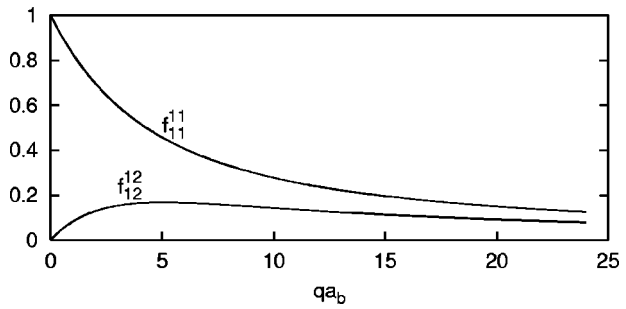

FIG. 16. Overlap integrals f_{11}^{11} and f_{12}^{12} as functions of dimensionless wave number qa_b.

$$I_{\mathbf{k}}^{ml}=\frac{1}{\hbar}\sum_{p,s,\mathbf{q}} V_{ls}^{mp}(\mathbf{k}-\mathbf{q})p_{\mathbf{q}}^{ps}=\frac{1}{\hbar}\frac{A}{(2\pi)^2}\int_0^\infty dq\int_0^{2\pi} d\varphi \times V_{ls}^{mp}(\mathbf{k}-\mathbf{q})p_{\mathbf{q}}^{ps} =\frac{E_b a_b}{\pi\hbar}\int_0^\infty dq\int_0^{2\pi} d\varphi\frac{f_{ls}^{mp}(q)}{\kappa+\sqrt{k^2+q^2-2kq\cos\varphi}}p_{\mathbf{q}}^{ps} =\frac{E_b a_b}{\pi\hbar}\int_0^\infty dq F_{ls}^{mp}(k,q)p_{\mathbf{q}}^{ps}, \tag{A1}$$

where we introduced the dimensionless function

$$F_{ls}^{mp}(k,q)=q\int_0^{2\pi} d\varphi\frac{f_{ls}^{mp}(q)}{\kappa+\sqrt{k^2+q^2-2kq\cos\varphi}}. \tag{A2}$$

For numerical integration we define the dimensionless wave numbers $\tilde{k}=ka_b$. We choose the upper limit $\tilde{k}_{\max}=12$ and divide the whole interval into $N=120$ parts with $\Delta\tilde{k}=\tilde{k}_{\max}/N$. We obtain

$$I_{\mathbf{k}}^{ml}\approx\frac{E_b\Delta\tilde{k}}{\pi\hbar}\sum_{\tilde{q}} F_{ls}^{mp}(\tilde{k},\tilde{q})p_{\tilde{q}}^{ps} \tag{A3}$$

with $\tilde{q}=0,\Delta\tilde{k},2\Delta\tilde{k},\ldots,\tilde{k}_{\max}$. The functions $F_{ls}^{mp}(k,q)$ are tabulated before integrating Eq. (3) in time. The behavior of the functions $F_{ls}^{mp}(k,q)$ is very important for understanding the origins of some of numerical errors in integrating Eq. (3). Figure 16 shows two overlap integrals $f_{11}^{11}(q)$ and $f_{12}^{12}(q)$. For the given QW parameters $L/a_b=0.968$. The overlap integral $f_{11}^{11}(q)$ starts at unity and decreases with increasing q. The overlap integral $f_{12}^{12}(q)$ increases from zero, reaches a maximum, and then decreases with increasing q. Similar behavior is obtained for other overlap integrals. For an infinitely thin QW, $L\ll a_b$, $f_{11}^{11}(q)=1$ and $f_{12}^{12}(q)=0$ independent of q. Figure 17 shows two functions $F_{11}^{11}(k,q)$ and $F_{12}^{12}(k,q)$, which correspond to the two overlap functions shown in Fig. 16, and the function $F(k,q)$ for the case of an infinitely narrow

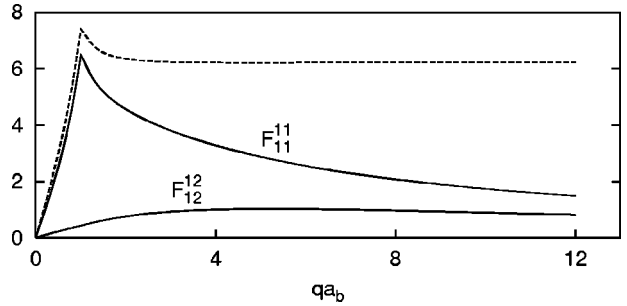

FIG. 17. Functions $F_{11}^{11}(k,q)$ and $F_{12}^{12}(k,q)$, which correspond to the overlap functions shown in Fig. 16, and the function $F_{11}^{11}(k,q)$ for the case of an infinitely narrow QW with unit overlap integral (dashed line) for a fixed value of $k=a_b^{-1}$.

QW (with unit overlap function). In evaluating these functions we assumed a small screening $\kappa a_b=0.1$. For an infinitely narrow QW without screening, the function $F(k,q)$ exhibits a logarithmic singularity at $k=q$ and approaches 2π as $q\rightarrow\infty$. The singularity is integrable and the introduction of small dephasing does not affect the results appreciably. However, the fact that the function is constant for large q gives rise to coupling of the polarization components with any value of k in Eq. (3) to all the polarization components extending far above the band gap. Even if an optical pulse is tuned near the band gap, it will excite all the polarization components lying far above the band gap and the contribution of the polarization components with some frequency ω decreases slowly, namely, $\sim(\omega_k-\omega_g)^{-1}$, which gives divergent macroscopic polarization in Eq. (11) and divergent Coulomb terms in Eq. (3). These artifacts are apparently inherent in the assumption of infinitely extended bands. Thus, a cutoff at a wave number of the order of the dimension of the Brillouin zone must be introduced. We also note that the results are rather sensitive to the position of the cutoff. However, for the cutoff used of $ka_b=12$, we checked that the results do not change if we use more integration points. From Fig. 17 we also see that the finite width of the QW gives rise to a decrease of F for large q.

*Present address: School of Electrical and Computer Engineering, Georgia Institute of Technology, Atlanta, GA 30332-0250.

[1] D. A. B. Miller, Int. J. Optoelectron. **11**, 155 (1997).
[2] S. Schmitt-Rink, D. S. Chemla, and D. A. B. Miller, Adv. Phys. **38**, 89 (1989).
[3] D. A. B. Miller, D. S. Chemla, and S. Schmitt-Rink, Phys. Rev. B **33**, 6976 (1986).
[4] For a review of recent developments in THz sources, see, for example, IEEE Trans. Microwave Theory Tech. **48**, No. 4 (2000), special issue on terahertz electronics.
[5] D. S. Lee and K. J. Malloy, IEEE J. Quantum Electron. **30**, 85 (1994).
[6] A. Liu and C. -Z. Ning, J. Opt. Soc. Am. B **17**, 433 (2000).
[7] S. H. Autler and C. H. Townes, Phys. Rev. **100**, 703 (1955).
[8] S. M. Sadeghi, J. F. Young, and J. Meyer, Phys. Rev. B **56**, R15 557 (1997).
[9] A. V. Maslov and D. S. Citrin, Phys. Rev. B **62**, 16 686 (2000).
[10] M. Artoni, G. C. La Rocca, and F. Bassani, Europhys. Lett. **49**, 445 (2000).
[11] J. Černe, J. Kono, T. Inoshita, M. Sherwin, M. Sundaram, and A. C. Gossard, Appl. Phys. Lett. **70**, 3543 (1997).
[12] J. Kono, M. Y. Su, T. Inoshita, M. Noda, M. S. Sherwin, S. J. Allen, Jr., and H. Sakaki, Phys. Rev. Lett. **79**, 1758 (1997).
[13] K. Johnsen and A.-P. Jauho, Phys. Rev. Lett. **83**, 1207 (1999).
[14] S. Hughes and D. S. Citrin, Phys. Rev. B **60**, 13 272 (1999).
[15] K. Johnsen, Phys. Rev. B **62**, 10 978 (2000).
[16] C. Phillips, M. Y. Su, M. S. Sherwin, J. Ko, and L. Coldren, Appl. Phys. Lett. **75**, 2728 (1999).
[17] A. V. Kuznetsov, G. D. Sanders, and C. J. Stanton, Phys. Rev. B **52**, 12 045 (1995).
[18] H. Haug and S. W. Koch, *Quantum Theory of the Optical and Electronic Properties of Semiconductors* (World Scientific, Singapore, 1998).
[19] V. I. Rupasov and V. I. Yudson, Sov. J. Quantum Electron. **12**, 1415 (1982).
[20] D. S. Citrin, Phys. Rev. B **47**, 3832 (1993).
[21] A. V. Maslov and D. S. Citrin, *Ultrafast Electronics and Optoelectronics*, OSA Technical Digest (Optical Society of America, Washington DC, 2001), pp. 39–41.
[22] A. V. Maslov and D. S. Citrin, *Ultrafast Electronics and Optoelectronics*, edited by Y-K. Chen, Wayne Knox, and Mark Rodwell, OSA Trends in Optics and Photonics, Vol. 49 (Optical Society of America, Washington DC, 2001), pp. 44–48.
[23] P. K. Tien and J. P. Gordon, Phys. Rev. **129**, 647 (1962).